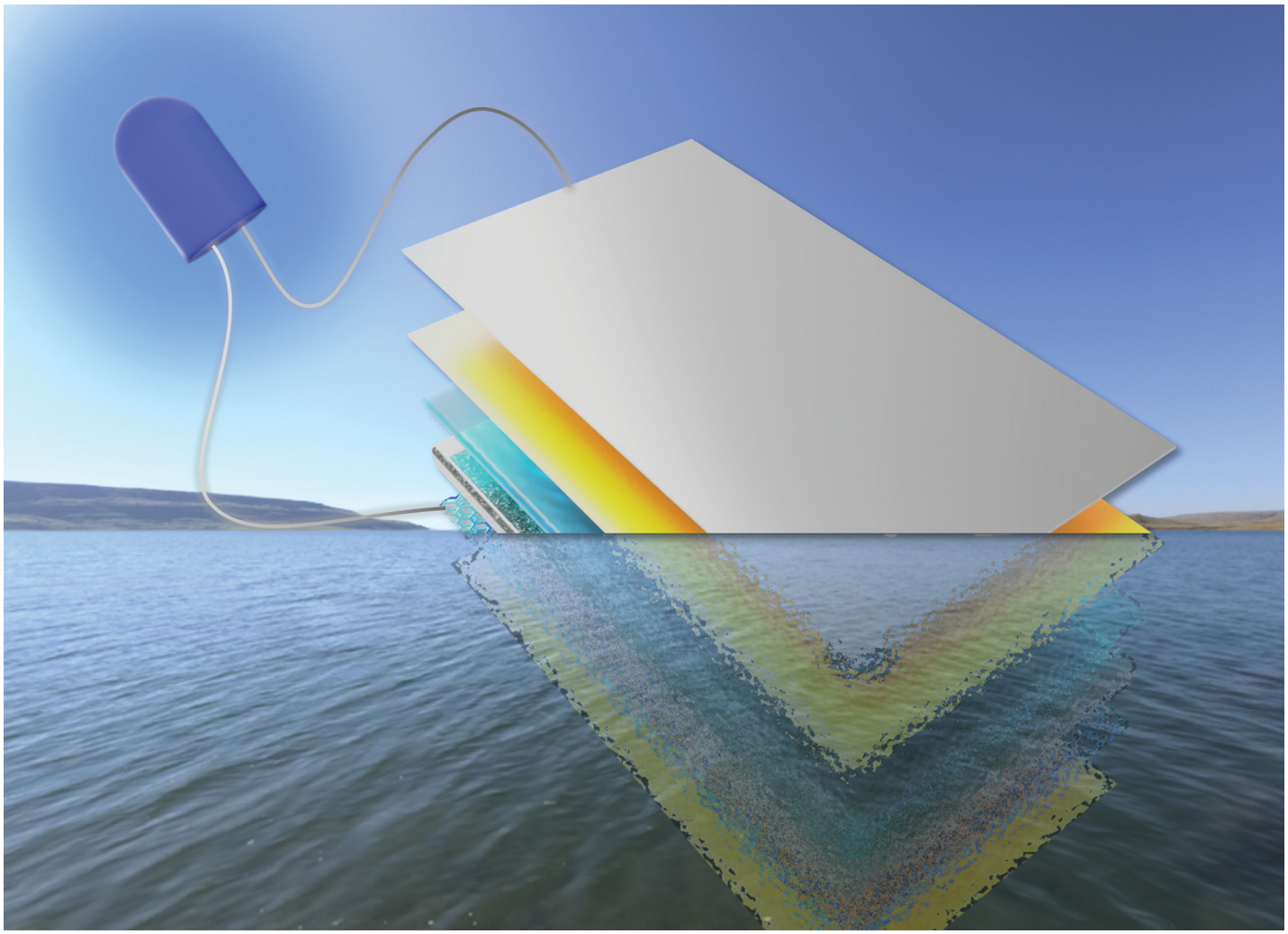

Showcasing research from Professor John A. Rogers's laboratory, Department of Materials Science and Engineering, Northwestern University, Evanston, Illinois, United States of America.

High performance dual-electrolyte magnesium–iodine batteries that can harmlessly resorb in the environment or in the body

Given the upward trajectory of global battery consumption, resulting waste streams cannot be overlooked. Spent batteries enter landfills at alarming rates and represent a growing societal challenge. This article describes a battery technology that addresses these challenges by exploiting the emerging class of physical transient biocompatible materials to offer capabilities that avoids the generation of any battery waste. The high-performance eco- and bio-resorbable magnesium–iodine battery powers a range of devices. Artwork was designed by Yamin Zhang.

As featured in:

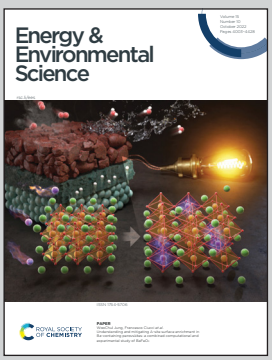

See Amay J. Bandodkar, John A. Rogers *et al.*, *Energy Environ. Sci.*, 2022, **15**, 4095.

ROYAL SOCIETY OF CHEMISTRY

rsc.li/ees

Registered charity number: 207890

Energy & Environmental Science

PAPER

View Article Online
View Journal | View Issue

Cite this: *Energy Environ. Sci.*, 2022, **15**, 4095

High performance dual-electrolyte magnesium–iodine batteries that can harmlessly resorb in the environment or in the body†

Ivy Huang, ‡[abc] Yamin Zhang, ‡[ab] Hany M. Arafa,[abd] Shupeng Li,[e] Abraham Vazquez-Guardado,[ab] Wei Ouyang,[ab] Fei Liu,[abc] Surabhi Madhvapathy,[abc] Joseph Woojin Song,[d] Andreas Tzavelis,[abd] Jacob Trueb,[ab] Yeonsik Choi,[ab] William J. Jeang,[ab] Viviane Forsberg,[abe] Elizabeth Higbee-Dempsey,[f] Nayereh Ghoreishi-Haack,[f] Iwona Stepien,[f] Keith Bailey,[g] Shuling Han,[hi] Zheng Jenny Zhang,[hi] Cameron Good,[ab] Yonggang Huang,[bcjk] Amay J. Bandodkar *[l] and John A. Rogers*[abcdjm]

Received 21st June 2022,
Accepted 30th August 2022

DOI: 10.1039/d2ee01966c

rsc.li/ees

Batteries represent the dominant means for storing electrical energy, but many battery chemistries create waste streams that are difficult to manage, and most possess toxic components that limit their use in biomedical applications. Batteries constructed from materials capable of complete, harmless resorption into the environment or into living organisms after a desired period of operation bypass these disadvantages. However, previously reported eco/bioresorbable batteries offer low operating voltages and modest energy densities. Here, we introduce a magnesium–iodine chemistry and dual (ionic liquid/aqueous) electrolyte to overcome these limitations, enabling significant improvements in voltage, areal capacity, areal energy, areal power, volumetric energy, and volumetric power densities over any alternative. Systematic studies reveal key materials and design considerations. Demonstrations of this technology include power supplies for cardiac pacemakers, wireless environmental monitors, and thermal sensors/actuators. These results suggest strong potential for applications where commercial battery alternatives pose risks to the environment or the human body.

[a] *Center for Bio-Integrated Electronics, Northwestern University, Evanston, IL, 60208, USA. E-mail: jrogers@northwestern.edu*
[b] *Querrey Simpson Institute for Bioelectronics, Northwestern University, Evanston, IL, 60208, USA*
[c] *Department of Materials Science and Engineering, Northwestern University, Evanston, IL, 60208, USA*
[d] *Department of Biomedical Engineering, Northwestern University, Evanston, IL, 60208, USA*
[e] *Department of Natural Sciences, Mid Sweden University, Holmgatan 10, 851 70, Sundsvall, Sweden*
[f] *Developmental Therapeutics Core, Northwestern University, Evanston, IL, 60208, USA*
[g] *Charles River Laboratories, Mattawan, MI, 49071, USA*
[h] *Comprehensive Transplant Center, Feinberg School of Medicine, Northwestern University, Chicago, IL, 60611, USA*
[i] *Department of Surgery, Feinberg School of Medicine, Northwestern University, Chicago, IL, 60611, USA*
[j] *Department of Mechanical Engineering, Northwestern University, Evanston, IL, 60208, USA*
[k] *Department of Civil and Environmental Engineering, Northwestern University, Evanston, IL, 60208, USA*
[l] *Department of Electrical and Computer Engineering, North Carolina State University, Raleigh, NC, 27606, USA. E-mail: ajbandod@ncsu.edu*
[m] *Department of Neurological Surgery, Feinberg School of Medicine, Northwestern University, Chicago, 60611, IL, USA*

† Electronic supplementary information (ESI) available: Effect of dual-electrolyte *vs.* conventional cell architectures, effect of ionic liquid on iodine release, additional figures of powering energy demanding electronics with the Mg–I2 eco/bioresorbable cell, statistical analysis of toxicologic pathology studies, surgical images of cell implantation *in vivo*, batch cell fabrication schematic, comparison tables against (1) eco/bioresorbable cells, (2) non-bioresorbable, implantable cells, and commercial, non-degradable cells and batteries. See DOI: **https://doi.org/10.1039/d2ee01966c**

‡ These authors contributed equally.

Broader context

Given the upward trajectory of global battery consumption, resulting waste streams cannot be overlooked. Spent batteries enter landfills at alarming rates and represent a growing societal challenge. Incorrectly disposed batteries can result in toxic materials leakage into ground water and soil, and the production of hazardous gas and accidental fires. This article describes a battery technology that addresses these challenges through the use of physically transient biocompatible materials that avoid the generation of any battery waste and enable power supplies for temporary biomedical implants or environmental monitors. Specifically, these high-performance magnesium–iodine eco- and bio-resorbable batteries completely dissolve in the presence of aqueous media, such as ground water, rainwater, or body fluids to resorb naturally and safely into the environment. The ionic liquid/aqueous media dual-electrolyte design enables eco/bioresorbable magnesium–iodine cells with voltage outputs and volumetric energy levels that exceed alternatives and meet power requirements for microcontrollers and Bluetooth devices.

Introduction

Global battery consumption continues to escalate, with a five-fold increase projected by 2030.[1] Given this upward trajectory, resulting waste streams from end-of-life alkaline and lithium-ion batteries cannot be overlooked. Currently, more than 95% of lithium-ion batteries (LIB) are sent to landfills.[2–7] LIB waste streams can be hazardous to the environment, as disposed battery casings and toxic organic electrolytes can leak into ground water and soil, with the potential to react violently with water and produce toxic gases such as hydrogen fluoride incidentally.[5] Alkaline zinc primary batteries contain corrosive potassium hydroxide electrolytes and manganese dioxide, which is a cumulative neurotoxin.[8] These components pose threats to the environment and public health if not disposed of appropriately and safely. Alternative battery chemistries and cell designs could bypass many of these concerns.

Battery toxicity concerns are also relevant for biomedical applications, particularly those in implantable devices, where failures can lead to severe complications and tissue damage.[9] In addition, emerging classes of temporary electronic implants[10–13] require batteries[14,15] that support operation for a medically relevant timeframe, often dictated by a biological process such as wound healing, and then disappear naturally due to processes of bioresorption to bypass the need for secondary surgical extraction.

Battery materials that fully degrade to harmless end products when exposed to ground water or biofluids[16,17] serve as the basis for 'physically transient' devices that naturally disappear to eliminate their load on the environment or on the body after a desired period of use.[18] Previously reported batteries of this type possess low operating voltages and/or low energy densities,[19–27] capable of powering only simple devices for purposes of demonstration. The most advanced example incorporates a magnesium–molybdenum trioxide (Mg–MoO_3) chemistry that can support operation of a light-emitting diode, a simple calculator, and a low-noise amplifier for benchtop measurement of electrocardiograms (ECGs).[21] None of these systems[19–27] can replace commercial batteries for miniature devices that require, for example, Bluetooth modules for wireless communication or specialized analog front end integrated circuits for multimodal sensors.

Here we introduce a collection of eco/bio-compatible materials and dual-electrolyte cell architectures as the basis for high performance, resorbable (>95% by weight) cells capable of powering various energy demanding biomedical and consumer electronic devices. Magnesium (Mg) possesses high theoretical capacity (2205 mA h g^{-1}) and low standard electrode potential ($Mg \Leftrightarrow Mg^{2+} + 2e^-$, $E^0 = -2.38$ V *vs.* Standard Hydrogen Electrode (SHE)), prompting widespread adoption as a battery anode, including Mg ion batteries[28] and Li–Mg dual-salt batteries (DSBs).[29,30] Mg represents a major body mineral (minimum daily intake: 100 mg day^{-1})[31] and participates in over 300 metabolic processes as a cofactor.[32] Moreover, Mg is commonly used in orthopedic implants[33,34] and cardiovascular stents[35] due to its excellent biocompatibility,[36] nontoxic products from corrosion,[34,36] and low thrombogenicity.[35] These reasons motivate our choice to utilize Mg as the anode. Iodine (I_2, 211.2 mA h g^{-1}) is an excellent choice for the cathode material because (1) it possesses a higher standard electrode potential ($I_2 + 2e^- \Leftrightarrow 2I^-$, $E^0 = 0.536$ V *vs.* SHE) and enables a higher voltage output of ~1.8 V in phosphate buffered solution (PBS) than other eco/bioresorbable options, such as Fe/Mo/W (~0.8/0.5/0.7 V)[20] and MoO_3 (~1.6 V);[21] and (2) it functions as an essential micronutrient[37,38] (0.15–1.11 mg day^{-1}) for a healthy thyroid and plays a significant role in medical treatments, commonly utilized as a topical antiseptic for wound care or on coatings of surgical implants[39] to prevent microbial infections. Both electrode materials also naturally occur in the environment and agronomic supplementation with these nutrients can improve crop health and yield.[40,41] I_2 is dispersed in carbon black to form the cathode. Carbon black represents <5% of the cell weight, and our studies (discussed later) demonstrate that the carbon released from the cell has no apparent effect on living organisms. Together, the electrode materials support a stable 1.8 V operating voltage at 0.4 mA cm^{-2} in PBS electrolyte, higher than a commercial 1.5 V alkaline battery and a 1.5 V Li-ion battery. Unlike previously reported examples that utilize ionic liquids (ILs) and aqueous electrolytes mixed as co-solvents,[42] the cells reported here exploit a partitioned dual-electrolyte system,[43] where the catholyte consists of a biocompatible choline chloride/urea-based IL and the ambient aqueous media serves as the anolyte. Mg corrodes at a rate of ~1.2–12 μm per day in simulated body fluids and at physiological conditions,[16] which corresponds to a hydrogen generation

rate of 8.6×10^{-6}–8.6×10^{-5} mol per day per cm^2. To allow release of hydrogen gas and, therefore, to eliminate gas blinding of the Mg anode, the analyte is composed of the body fluid or an aqueous fluid open to the surroundings. Two holes in a polyanhydride membrane that separates these two liquids define the liquid–liquid interface. This design yields greatly enhanced durability and improved capacity compared to analogous systems that use a single electrolyte (only IL or only aqueous media) or a mixture of IL and an aqueous fluid. A polymeric encapsulation around the cathode and IL reduces I_2 dissolution and minimizes H_2 gas poisoning[44] from dissolution of the Mg.

Selection of materials for the encapsulation structure and the electrolyte follow similar considerations. The former relies on polyanhydride (PA), a polymer that readily hydrolyzes into environmentally and biologically safe dicarboxylic acids in the presence of aqueous media.[45,46] Toxicity investigations of several cholinium-based deep eutectic ILs reveal that choline-chloride based materials are biodegradable[47] with antibacterial properties, beneficial to living systems and the environmental applications.[48]

The dual-electrolyte cell architecture ensures that quantities of all components remain within a safe recommended daily range. For instance, a cell with $\sim$10 mA h cm^{-2} capacity utilizes $\sim$12 mg Mg, $\sim$22 mg I_2 and $\sim$6 mg PA. The US Food and Drug Administration (FDA) recommends a Daily Value of 420 mg of Mg,[49] and Mg supplements usually contain 250–500 mg of Mg. According to the fact sheet provided by the National Institutes of Health (NIH) Office of Dietary Supplements (ODS), the average daily recommended amount of iodine for adults is 0.15–0.29 mg day^{-1}. The PA pouch reduces the iodine release rate to $\sim$0.19 mg day^{-1}, which falls into the average daily recommended range and well below the upper recommended limit of 1.1 mg day^{-1}.[50]

To summarize, the uniqueness of the battery technology introduced here follows from its (1) nearly exclusive use of eco/bioresorbable materials, (2) dual IL/aqueous electrolyte cell architecture, and (3) superior output voltage, areal capacity, areal energy, areal power, volumetric energy, and volumetric power densities. Demonstration examples that leverage these characteristics include wireless wearable systems, microcontrollers, temperature sensors, resistive heating elements, and cardiac pacemakers. The results suggest promise for applications in devices that bypass requirements for management of solid waste streams and in temporary biomedical implants that avoid the need for surgical extraction.

Results

Design of the eco/bioresorbable cell

Fig. 1a and b schematically illustrate the essential components of the eco/bioresorbable cell and its operating principles. Mg foil represents an ideal choice as an anode because it features the lowest standard electrode potential among other eco/bioresorbable metals (iron (Fe), zinc (Zn), molybdenum (Mo), tungsten (W))[51] and it possesses a high volumetric energy density (3833 mA h cm^{-3}). To avoid the low operating voltages ($<$1 V at 0.1 mA cm^{-2})[20] that result from direct coupling of Mg with eco/bioresorbable metal cathodes (Fe, Mo, W), the cells reported here use the highly electropositive material I_2, for achieving operating voltages $>$1.8 V. Previously reported Mg–I_2 cells rely on toxic organic electrolytes,[28] which prevent their use in biomedical devices and additionally create environmental hazards.[52,53] Moreover, such cells usually require specialized, non-degradable casings that contribute to solid waste streams and prevent use in bioresorbable implants. Our approach with dual IL/aqueous electrolyte allows the Mg–I_2 chemistry to circumvent these concerns by operating without organic electrolytes.

Although I_2 is electronically insulating, mixing the I_2 with 8 wt% carbon black and 17 wt% of a blend of bioresorbable chitosan and poly(lactide-*co*-glycolide) (PLGA) forms a conductive composite that, when bonded to a 15 μm Mo foil or 20 mesh Mo gauze, overcomes this limitation. The carbon black imparts conductivity and minimizes leaching of I_2 due to strong adsorptive properties.[54] The water permeability of the PLGA enhances the effective surface area of the I_2 in the composite and forms a 3D porous network, thereby improving the cell performance.[21] The chitosan exhibits a strong affinity to I_2[55] and its amine and hydroxyl groups form a water barrier[56–58] that prevents rapid I_2 dissolution. While sufficient for applications that require operation for $<$24 h, additional modifications to this design, detailed below, extend the lifetime to at least 7 days.

The key modification involves the use of a hydrophobic pouch of PA to contain the ChCl/urea-based IL. Measurements show that I_2 dissolution occurs at lower rates in the dual IL/aqueous electrolyte than in the aqueous electrolyte alone, as discussed in detail subsequently. The results enable stable operation even after soaking in aqueous media for 7 days. The cells reported in the following use five microliters of IL[59] prepared from melting 1 : 2 moles of ChCl and urea (molten salt) with 0.3 M of zinc chloride ($ZnCl_2$), where $ZnCl_2$ supplies ions needed to support conductivity.

Configuring two inlets (diameter: 750 μm, Fig. S1, ESI†) on the upper surface of the pouch facilitates the liquid–liquid interface of the catholyte (IL) inside the pouch with the anolyte comprised of the surrounding aqueous media (*e.g.* biofluid or ground water) (Fig. 1c). Redox reactions lead to the formation of hydroxide and hydrogen gas byproducts at the Mg anode. Placing this electrode outside the pouch prevents the buildup of these byproducts from stifling the electrochemical reactions. The thickness of the Mg must be sufficient to accommodate corrosion processes that follow from exposure to aqueous electrolyte (Fig. S2, ESI†). The examples reported here use foils with thicknesses of 200 μm. Placing the Mg foil atop the PA pouch forms a complete cell (Fig. 1d and Fig. S3a, ESI†) with compact size ($5.2 \times 5.2 \times 1.9$ mm^3), low weight ($\sim$46 mg) and high areal capacity ($\sim$10 mA h cm^{-2}). Fig. 1e and Fig. S3b (ESI†) present schematic illustrations of a conventional Mg–I_2 cell, to illustrate the key design differences.

Experiments to demonstrate processes of dissolution relevant to uses in temporary biomedical implants involve

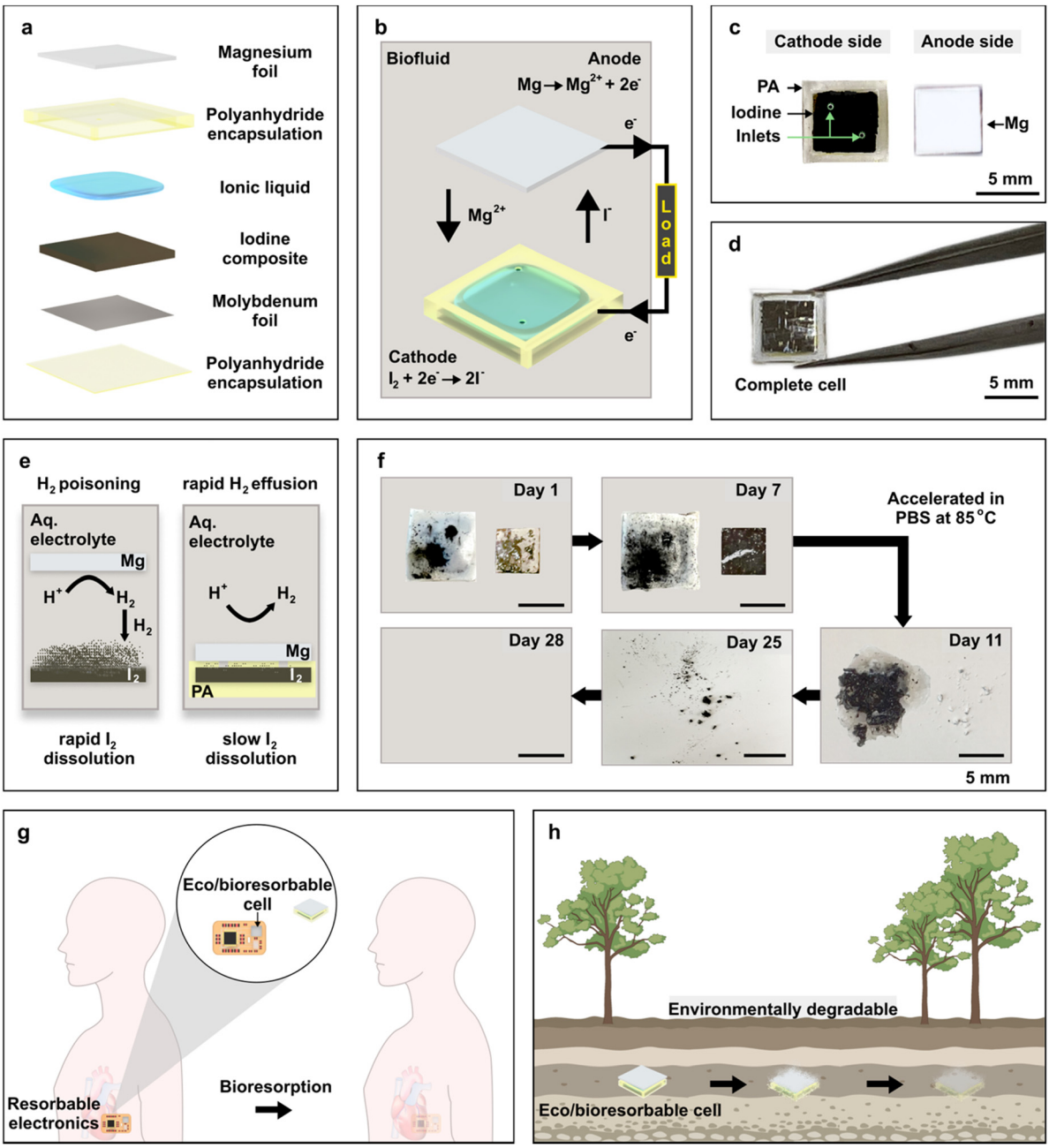

Fig. 1 Materials, chemistry and design features of a high performance, eco/bioresorbable cell. (a) Schematic exploded view illustration of the dual-electrolyte based Mg–I_2 cell. (b) Schematic diagram of the redox chemistry, illustrating the electrochemical reactions at the magnesium anode and iodine cathode when submerged in biofluid or ground water (electrolyte). This type of device can support operation of various classes of conventional electronic devices, including thermal sensors and actuators, pacemakers, wireless communication modules and microcontrollers. (c) Optical images of the cathode and anode, laterally placed. The green arrows point to inlets on the surface of a polyanhydride encapsulation structure. Scale bar, 5 mm. (d) Optical image of a cell, vertically stacked. Scale bars, 5 mm. (e) (left) Conventional Mg–I_2 cell and (right) eco/bioresorbable cell in dual IL/aqueous electrolyte. The conventional Mg–I_2 cell experiences rapid I_2 dissolution and is affected by the H_2 gas production originating from the anode, whereas the dual-electrolyte cell does not, due to the addition of encapsulation and the ionic liquid electrolyte. (f) Optical images at various stages of the dissolution of a cell associated with immersion in PBS (pH 7.4). Days 0-7:37 °C, Days 7-28:85 °C. The entire cell naturally degrades. Scale bars, 5 mm. (g and h) Proposed utilization of the eco/bioresorbable battery. (g) Resorbable electronics powered by the eco/bioresorbable cell implanted in the human body jointly degrade without an adverse reaction after performing the designated function. (h) The eco/bioresorbable cell naturally degrades in soil and ground water after use, and disposal of these cells do not produce an adverse reaction on environmental health.

immersion in PBS solution (pH 7.4) at physiological temperature (37 °C) (Fig. 1f). Degradation occurs most rapidly *via* hydrolysis of Mg (0.05–0.5 μm h^{-1} in physiological conditions)[16,45,60] and PA (10^{-2} μg day^{-1} in physiological conditions),[45,46] followed by dissolution of I_2 into ions and finally with comparatively slow hydrolysis of Mo (10^{-4}–10^{-3} μm h^{-1} at room temperature).[16,45,61] The observed degradation behavior agrees with previous reports in the context of bioresorbable electronic devices.[16,45,60,61]

Encapsulating the entire Mg–I_2 cell with a stimuli-responsive bioresorbable material offers a potential means to initiate the transience of the cell[62] based on exposure to heat[63] or UV light,[64] as examples. The discharge process accelerates the degradation of the Mg–I_2 cell because (1) the Mg anode oxidizes under discharge, in addition to its natural degradation, and (2) I_2 reduces to I^- during discharge, then reacts with I_2 and forms I_3^-, which has a higher leaching rate than I_2.[65]

Some envisioned use cases appear in the illustrations of Fig. 1g and h. In one case, the cell powers a temporary electronic implant (Fig. 1g). After addressing a medical need, the entire system, including the cell, safely dissolves completely to eliminate the risks and costs associated with a secondary surgery for retrieval. In another example (Fig. 1h), the cell powers a consumer electronic device or an environmental monitor. Here, the cell degrades in soil in the presence of ground water or rainwater and naturally disappears without waste streams or adverse effects on the environment.

Electrochemical properties and performance characteristics

Fig. 2a presents scanning electron microscope (SEM) images of the I_2 cathode and results of energy dispersive X-ray spectroscopy (EDS), both confirming the uniform distribution of I_2 within the carbon black matrix. Fig. S4a (ESI†) presents a schematic illustration of the dual-electrolyte cell and a conventional Mg–I_2 cell to highlight the differences. To connect the electrodes to the external circuit, a laser-patterned tab affixed to the body of the electrode provides an electrical connection to conductive wires through application of Ag conductive epoxy (Fig. S4d and e, ESI†). Fig. 2b displays discharge profiles for cells with fixed Mg anode thickness (200 μm) and different mass loadings of I_2 in the cathode at a constant current discharge (CCD) of 0.4 mA cm^{-2}. The operating voltage is >1.8 V, significantly higher than previously reported cells.[19–27] Experiments on Mg–I_2 cells in the dual-electrolyte (Dual) and in the single aqueous electrolyte (PBS) setups reveal the role of the IL. At 89 mg cm^{-2} I_2, the cell with the dual electrolyte (Dual-89) supports a discharge capacity of $\sim$3.9 mA h cm^{-2}, which is twice as high as that of a Mg–I_2 cell with PBS electrolyte and the same amount of I_2 (PBS-89, $\sim$1.9 mA h cm^{-2}). The mass of active material defines the capacity, such that in otherwise identical cells, 182 mg cm^{-2} I_2 (Dual-182) supports $\sim$10.1 mA h cm^{-2} at a CCD of 0.4 mA cm^{-2}. Immersing Mg–I_2 cells at 37 °C in PBS and discharging at different days after incubation yields data on changes in the voltage and capacity after activation by the anolyte. Fig. 2c and Fig. S4f (ESI†) reveal the effect of incubation time on the cell capacity and voltage for fully assembled batteries. Preservation of I_2 in the IL yields durable operation when incubated over a period of 7 days at 37 °C in PBS (Fig. 2c). By contrast, the cell with the single PBS electrolyte fails after only 1 day of incubation. Ultraviolet-visible (UV-vis) spectroscopy indicates that the IL reduces the rate of I_2 leakage from the electrode to the electrolyte (Fig. S4b and c, ESI†). The voltage and capacity decrease from 2 V and 3.9 mA h cm^{-2} at day 0 to 1.5 V and 0.3 mA h cm^{-2} at day 7, respectively, for the Mg–I_2 cells in the dual-electrolyte setup, which corresponds to a self-discharge rate of $\sim$13% per day. The battery capacity depends on the amount of electrode materials (Mg and I_2). The US Food and Drug Administration (FDA) recommends a daily value of 420 mg of Mg for adults.[49] A cell with 420 mg of Mg has a theoretical capacity of 926 mA h, allowing for safe implantation in an adult, under scenarios where the I_2 release rate is maintained below 0.29 mg day^{-1}, the maximum daily amount as recommended by the National Institutes of Health (NIH) Office of Dietary Supplements (ODS). Studies in this paper utilize the 89 mg cm^{-2} Mg–I_2 cell to reduce bodily exposure to implanted I_2, although batteries envisioned for environmental applications can increase the I_2 dose. When the cell is discharged at a constant voltage (0 V) using chronoamperometry (CA), the cell delivers an areal capacity of $\sim 13.4 \pm 2$ mA h cm^{-2} (Fig. 2d), which decreases to $\sim 5.2 \pm 0.1$, $\sim 2.1 \pm 0.7$, and $\sim 0.7 \pm 0.8$ mA h cm^{-2} after incubating in PBS for 1, 3, and 5 days, respectively, mainly due to degradation of the Mg anode. Fig. S4g (ESI†) presents the results of linear sweep voltammetry measurements. The data indicate that the eco/bioresorbable cell can operate at discharge currents greater than 4 mA cm^{-2}. Finite element analysis (Fig. 2e) illustrates that the charge concentrates around the edge of holes during discharge.

Fig. 2f presents a radar plot of key performance metrics (voltage, areal capacity, areal energy, areal power, volumetric energy, and volumetric power densities) of the battery technology reported here and those of previously reported eco/bioresorbable cells.[19–27] All calculations related to this battery utilize a discharge current of 0.4 mA cm^{-2}. Details appear in the ESI.† The operation voltage ($\sim$1.8 V), the areal capacity ($\sim$9.8 mA h cm^{-2}), the areal energy density ($\sim$17.7 mW h cm^{-2}), the areal power density ($\sim$0.7 mW cm^{-2}), the volumetric energy density ($\sim$93.0 mW h cm^{-3}), and the volumetric power density ($\sim$3.8 mW cm^{-3}) are all significantly higher than those of alternatives, as listed in Table S1 (ESI†). This summary does not include gravimetric parameters (*e.g.* specific capacity) due to a lack of available information (*e.g.* battery weight) in previous publications. The improved properties of the Mg–I_2 battery introduced here follow from the use of (1) Mg as a metal anode with high theoretical specific energy density (2205 mA h g^{-1}) and low standard electrode potential ($E^0 = -2.38$ V *vs.* SHE); (2) I_2 as a cathode with high standard electrode potential ($E^0 = 0.536$ V *vs.* SHE) compared to other bioresorbable alternatives; (3) a dual-electrolyte system, designed to reduce I_2 dissolution and preserve I_2 in the cathode. Additional comparisons (Fig. S5, ESI†) against non-bioresorbable, implantable cells suggest that the battery technology reported here could be advantageous over existing technologies (Table S2, ESI†).[19,23,24,26,27] The high-performance results of these eco/bioresorbable cells motivate additional comparisons against commercial primary cells, with the following guidelines (1) full cell comparisons that include electrodes, electrolyte, separator, and package material and (2) commercial cells with sizes that are closest to those of the cells introduced here. Fig. 2g and Table S3 (ESI†) detail the volumetric and gravimetric comparisons on voltage, volumetric energy density, volumetric capacity, specific energy density, and specific capacity based on datasheets supplied by battery manufacturers. The eco/bioresorbable batteries discussed here represent promising alternatives to Li-ion batteries

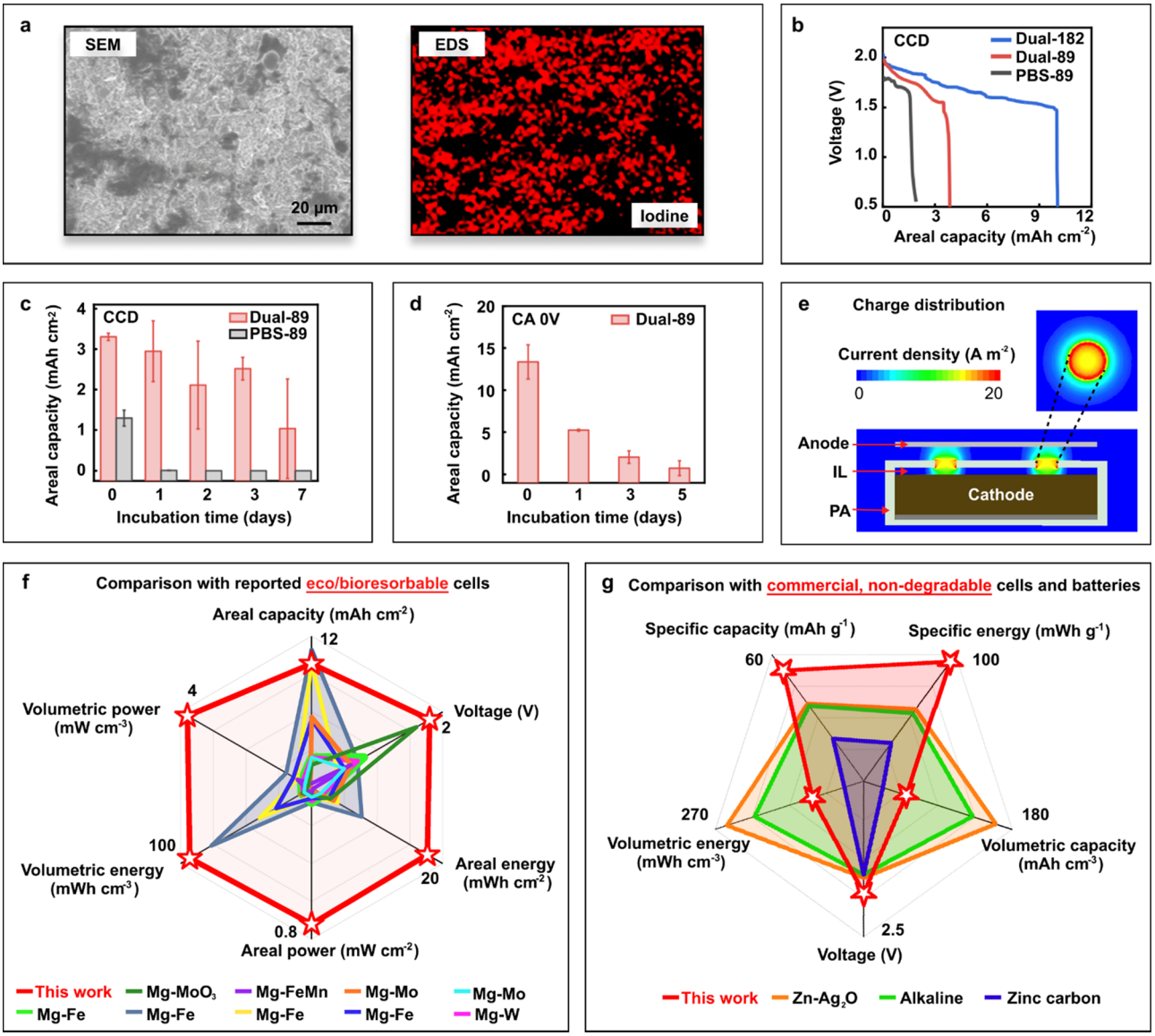

Fig. 2 Electrochemical properties and performance characteristics. (a) SEM and EDS mapping of an I_2 cathode. Scale bar, 20 μm. (b) Plots of discharge behaviors of conventional (PBS) and dual-electrolyte cells at different mass loadings of iodine (89 mg cm^{-2} and 182 mg cm^{-2}). Setting: Constant Current Discharge (CCD) of 0.4 mA cm^{-2}. n = 3 cells per group. (c) Effect of incubation time on the areal capacity of conventional (PBS) and dual-electrolyte cells after implantation in chicken breast and immersion in PBS (pH 7.4) at 37 °C. Setting: CCD of 0.4 mA cm^{-2}. n = 3 cells per day. (d) Effect of incubation time on the areal-capacity of dual-electrolyte cells immersed in PBS (pH 7.4) at 37 °C. Setting: chronoamperometry (CA) 0V. n = 3 cells per day. (e) FEA result for the current density distribution of the dual-electrolyte cell. (f and g) Radar plot comparison of performance characteristics of the battery technology reported here and (f) other eco/bioresorbable ($Mg–MoO_3$,[21] Mg–FeMn,[25] Mg–Mo(1),[21] Mg–Mo(2),[20] Mg–Fe(1),[22] Mg–Fe(2),[22] Mg–Fe(3),[22] Mg–Fe(4),[20] $Mg–W$[20]) and (g) commercial cells and batteries.

for applications that require modest amounts of power, such as implantable devices, wearable sensors, and environmental monitors. These cells, in their current form, provide specific capacities, specific energy densities and voltages that are ~1.5, ~1.8, and ~1.2 times greater than those of commercial alkaline zinc batteries in similar sizes. Opportunities for further improvement are in replacing the Mg anode with Mg alloys, to slow the rates of corrosion, and in optimizing the composition of the cathode.

In vivo operation and biocompatibility

The capacity to operate *in vivo* is an important feature of the described technology.[9,14] Fig. 3a illustrates application in a small-animal (rat) model. The eco/bioresorbable cell inserts through an incision in the intrascapular region and wired interconnects pass subdermally to a headcap for electrical access. A commutator interface minimizes mechanical stresses on the animals and transmits daily measurements of cell capacity after 0, 1, 3 and 5 days of implantation (Fig. 3b). Fig. S6 (ESI†) summarizes the details. At day 0, the capacity is ~15 ± 2 mA h cm^{-2}, which decreases to ~11 ± 0.2, ~5 ± 0.5, and ~1 ± 0.6 mA h cm^{-2} after 1, 3, and 5 days, respectively. The capacity gradually decays, likely due to the loss of electrical connection to the corroded Mg anode and/or to loss of ionic conduction (inlets) between the electrodes as a result of

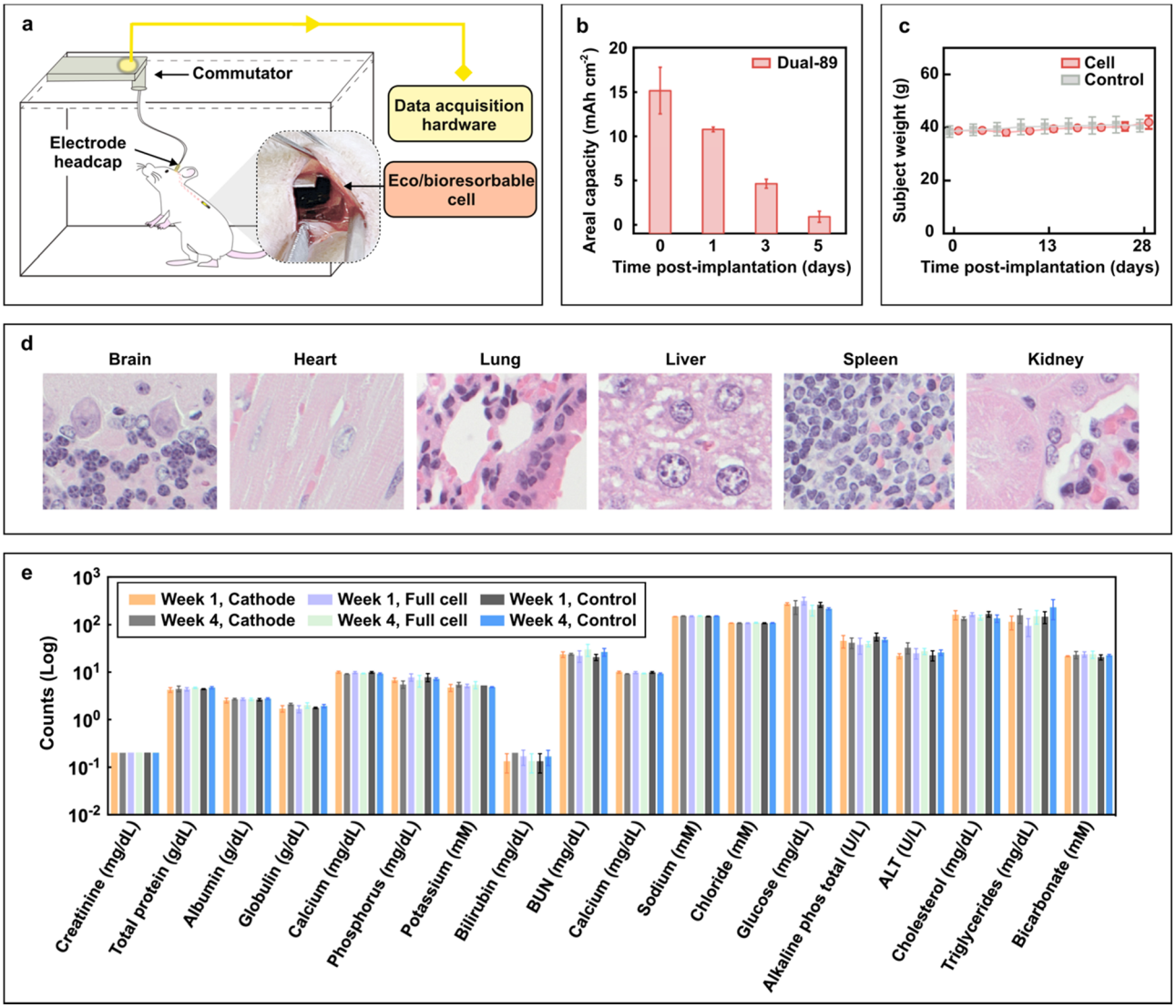

Fig. 3 *In vivo* study of cell capacity, biocompatibility, and toxicity. (a) Schematic diagram of a setup that supports areal capacity measurements within a cage environment. (b) Effect of *in vivo* incubation on the areal-capacity of dual-electrolyte cells implanted under the skin on the back of the animal. Iodine cathode: 89 mg cm^{-2}. Setting: chronoamperometry 0 V. n = 2 independent animals per day. (c) Weights of animals implanted with a cell or with a piece of PA (control) measured approximately every 3 days. Weights initially decrease post-surgery but increase appropriately with age thereafter, as expected in healthy animals. n = 3 independent animals per group. (d) Histological sections, indicating no evidence of systemic toxicity for the brain, heart, lung, liver, spleen or kidney (left to right) 4 weeks post-implantation. n = 3 independent animals per group. (e) Results of complete blood counts and blood chemistry for mice implanted with cathode, cell, and PA (control) at Weeks 1 and 4 reveal overall healthy physiology. n = 3 independent animals per group. ALT, alanine aminotransferase; GGT, gamma-glutamyl transferase; BUN: blood urea nitrogen. Displayed in log scale.

increasing buildup of oxides at the interface. Surface coating the Mg with nanocomposite hydroxyapatite can significantly reduce the corrosion rate of Mg[66] for improving performance.

Measurements of the weight of animals implanted with cells to those implanted with similarly sized pieces of PA reveal small initial declines, typical following surgeries, accompanied by a gradual increase over time, as expected in healthy animal models. Both the cell and control groups present similar weight trends (Fig. 3c). Evaluating the external surfaces and orifices, the body condition, the musculoskeletal system, and body cavities with associated organs and tissues of mice implanted with cells, I_2 cathode only, and PA only control groups on a 5-grade scoring system (Fig. S7 and S8, ESI†) reveal no evidence of systemic toxicity after 1 week and 4 weeks of implantation (Fig. 3d). Comparisons against the control groups demonstrate that organ weights are not statistically different than the treatment groups ($P > 0.05$; Fig. S9, ESI†). Further comparison and histological examination of the I_2 cathode and cell groups against the PA controls at 1 and 4 week (Fig. S10, ESI†) present no significant differences. Local hydrogen gas cavities are not observed in the mice implanted with cells, which is likely due to the relatively slow rate of hydrogen generation

and its fast escape rate through surrounding tissues.[67] No adverse effects are noticed due to gas generation from Mg corrosion, consistent with previous reports.[37,68] Results of serological tests summarized in Fig. 3e provide additional evidence of the biocompatibility of the battery technology introduced here.

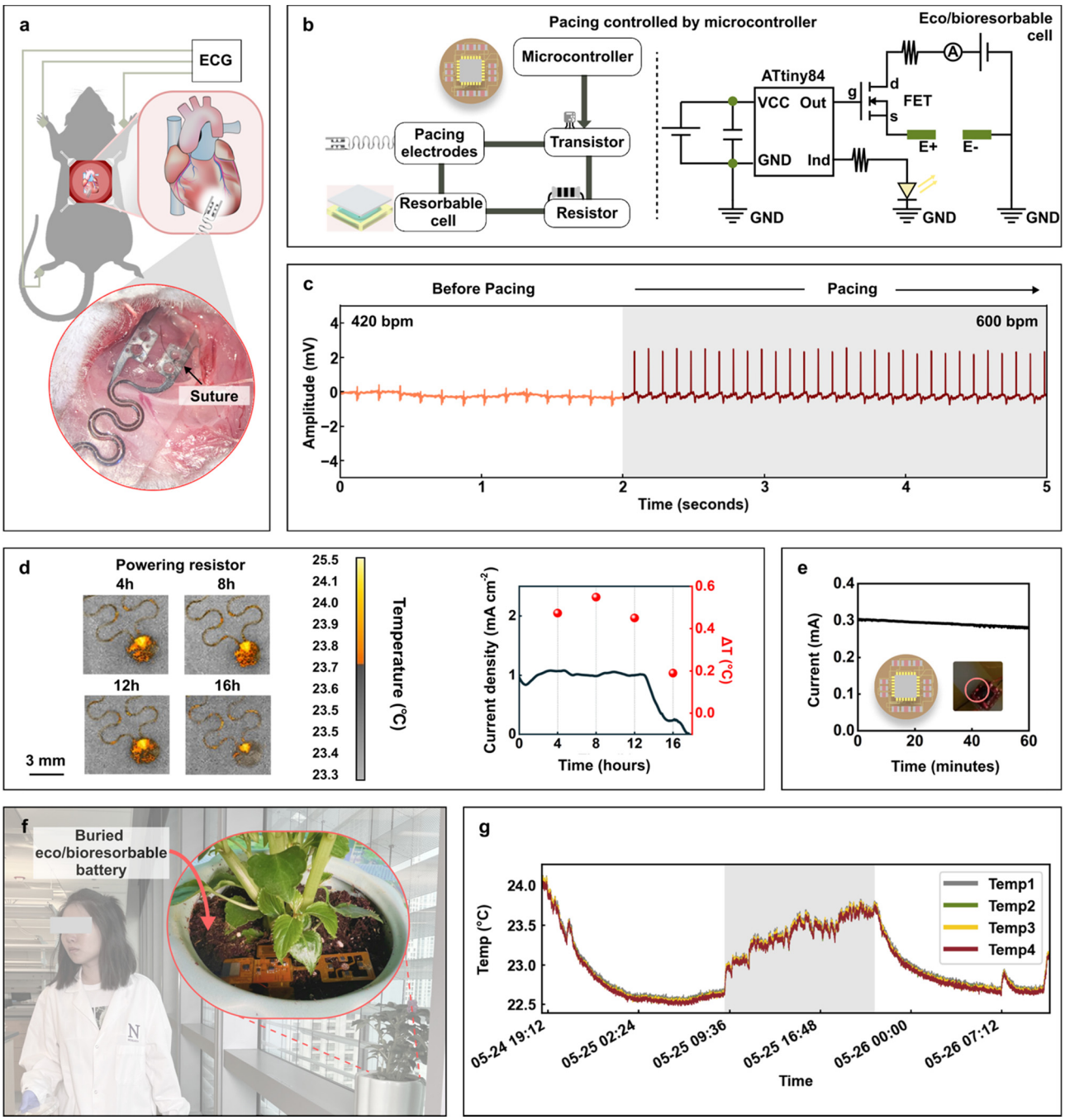

Fig. 4 Power supply for representative applications. (a) Schematic illustration of test setup in a small-animal model for cardiac pacing and ECG recording *via* subdermal needle electrodes positioned in Lead I configuration. Molybdenum electrodes laminated on the myocardial surface of the left ventricle and secured with sutures serve as the pacing leads. (b) (left) Operational diagram and (right) circuit schematic for a system that supports cardiac pacing using a microcontroller, powered with a single eco/bioresorbable cell. (c) ECG signals before (plain background) and during electrical stimulation (shaded background) with the eco/bioresorbable cell. Pacing in a healthy small-animal model. (d) Infrared images and current density for a resistive element powered by a single eco/bioresorbable cell and collected over the duration of its operational lifetime. Scale bar, 3 mm. (e) Demonstration of a single eco/bioresorbable cell powering an ATtiny84 microcontroller. (f) Photographs of the Bluetooth Low Energy (BLE) system on a chip (SoC) powered by a buried eco/bioresorbable battery placed inside a potted plant, capturing real-time measurements of nearby researchers. (g) Four simultaneous temperature measurements captured by a SoC powered by a eco/bioresorbable battery (two in series) implanted in ground water and soil.

Diverse applications with the eco/bioresorbable cells

The power levels, energy densities, and voltages supplied by these cells can support diverse applications (Fig. S11, ESI†). Examples presented here include cardiac pacemakers (Fig. 4a–c), sensors and heaters for thermal therapeutics, (Fig. 4d and e), and wireless environmental monitors (Fig. 4f and g).

Cardiac pacemakers provide electrotherapy to address cardiac disorders,[9] typically in the form of devices that combine battery-powered pacing electronics and pacing leads as tissue interfaces.[9,69–71] Temporary pacemakers, often used during a recovery period following a cardiac surgery, use leads that pass through the skin and connect to external power sources for stimulation. An alternative, based on bioresorbable leads powered using an implanted cell of the type introduced here, would eliminate these external tethers as well as the surgical extraction process needed to remove the leads. Initial characterization studies performed use raw chicken breast immersed in PBS to demonstrate feasibility, as summarized in Fig. S12 (ESI†). The schematic illustration in Fig. 4a highlights the setup for experiments in a mouse. Trials involve the animal under light sedation, with subdermal needle electrodes inserted in a Lead I configuration to capture ECG signals. An incision in the intercostal space provides access to the thoracic cavity (Fig. S13, ESI†). An image captured during a pacing trial shows a pair of Mo electrodes sutured to the anterior myocardial surface of the left ventricle. Fig. 4b presents an operational diagram and corresponding circuit schematic based on commercially available components, each of which can be realized in bioresorbable forms using concepts described previously.[72] Pacing uses a microcontroller with a pulse width of 2 ms that occurs every 0.1 s, to pace at a rate of 600 bpm (Fig. S14, ESI†). Successful ventricular rapid pacing drives the heart rate from 420 bpm to 600 bpm and appears in ECG traces with shortened R–R intervals in Fig. 4c.

Temporary implantable systems for thermal therapy[73,74] or continuous flow monitoring[12,75–77] represent additional areas of application. In the former, localized Joule heating delivers a known quantity of thermal power to a targeted tissue, such as that associated with a tumor, as a hyperthermia treatment at temperatures between 39–45 °C,[73] for time periods from seconds to hours depending on the requirements. In the latter, mild heating can be used for measurement of hydration state[76,78] or micro[79] or macrovascular[79,80] flow based on principles of calorimetry[81] or anemometry.[82] In Fig. 4d, the cell supplies a current density of $\sim$1 mA cm^{-2} for over 12 hours to a resistive heating element that has soft mechanical properties for efficient thermal coupling to the tissue.[75]

In many areas of application, wireless systems and microcontrollers are required to support operational requirements. As a demonstration of high voltage characteristics of the battery reported here, a single cell powers a microcontroller (ATtiny84) continuously for over an hour while delivering a stable output of 0.3 mA at 1.8 V in Fig. 4e, which has previously not been achievable without relying on boost converters or other additional electronic components. In another example, two cells in series supply power directly to a Bluetooth Low Energy (BLE) system on a chip (SoC). Fig. 4f presents an example of a BLE-enabled wireless sensor connected to the battery immersed in soil and ground water, as an example of an environmental monitor. The SoC acquires and wirelessly transmits data from four digital temperature sensor integrated circuits (sampling frequency of 64 Hz) and one inertial measurement unit (IMU), which includes both an accelerometer and an integrated temperature sensor (sampling frequency of 1600 Hz). Fig. 4g and Fig. S15 (ESI†) show measurements from the four temperature sensors and from the accelerometer, respectively, for the case of a device deployed in a potted plant located near the lab. Temperatures increase at 9:36 AM and stabilize at $\sim$9:00 PM, corresponding to increasing foot traffic corresponding to researchers entering the lab and leaving for the day, illustrating the environmental monitoring capabilities. The accelerometer in the IMU captures vibrations associated with the movements of researchers in the lab. Fig. S16 (ESI†) displays photographs of the custom graphical user interface (GUI) which wirelessly receives real-time measurements of the temperature and accelerometry measurements.

Conclusions

This paper introduces a Mg–I_2 chemistry, coupled with the dual IL/aqueous electrolytes cell architecture system, that enables eco/bioresorbable batteries with properties significantly better than alternatives. Systematic studies establish the basic materials considerations and motivate key design choices. Demonstration experiments highlight the practical potential of this technology. Enabled applications range from temporary electronic implants that obviate the necessity for surgical extraction after a period of medical need to remote environmental monitors that do not require recovery following their deployment. The performance characteristics of these batteries also suggest broad uses across different classes of consumer electronics gadgetry and industrial systems, with benefits in reduced waste streams and associated adverse environmental impacts. Many applications demand improved battery lifetime, perhaps realizable through bioresorbable encapsulating packages designed to delay the penetration of surrounding aqueous electrolyte and therefore time of battery activation. A collection of batteries with different package designs of this type may allow for a staged sequence of activation as the basis for continuous operation over an extended period of time. This direction and others represent promising routes to improve on the designs introduced here.

Materials and methods

Fabrication of the eco/bioresorbable cells

The cells used metal foils Mo (15 μm thick) and Mg (200 μm thick) purchased from Alibaba, and Mo gauze (20 mesh) purchased from Alfa Aesar. An ultraviolet laser (LPKF U4) defined the shapes of the anodes and cathodes. Mixing 9 : 1 ball-milled iodine (Sigma) and super P (MTI) with 600 μL of 300 mg mL^{-1} poly(D,L-lactide-*co*-glycolide) (PLGA) 65 : 35 M_w 40–75k (Sigma) in ethyl acetate and 800 μL of 3 wt% HMW chitosan in 1 M acetic acid within a planetary mixer (Thinky ARE-30;

10 min mix) formed a uniformly distributed slurry for the cathode. Positioning Mo foils/gauze in the trenches of a 3D printed mold, followed by orthogonally aligning a 3D printed spatula against the length of the foils, yielded 5 mm × 5 mm pockets to support batch production of the cathodes. Subsequent application of the slurry inside the pockets and atop the Mo foil completed the composite cathodes (Fig. S17, ESI†). Removing the structures from the 3D-printed mold, baking them at 65 °C for 30 min and then dip-coating in a 300 mg mL^{-1} PLGA solution and finally baking at 65 °C for 15 min completed the process.

Synthesis of polyanhydride (polybutanedithiol 1,3,5-triallyl-1,3,5-triazine-2,4,6(1*H*,3*H*,5*H*)-trione pentenoic anhydride, PA) following previously reported protocols[45] yielded films for the pouch. The synthesis began with cross-linking a 1 : 4 : 7 molar ratio of 4-Pentenoic Anhydride (Sigma), 1,3,5-triallyl-1,3,5-triazine-2,4,6(1*H*,3*H*,5*H*)-trione (Sigma), 1,4-Butanedithiol (Sigma) by illumination of UV light (intensity 590 μW cm^{-2}; wavelength of 365 nm) for 5 min, with 2,2-dimethoxy-2-phenylacetophenone (total mass of 0.5%; Sigma) as the photo-initiator to generate the eco/bioresorbable PA. Pouring silicone (Ecoflex 00-35, Smooth-On Inc., USA) atop a 3D printed mold (Form 3B, Formlabs) formed a patterned, soft silicone mold for the target structure. Adhering a glass slide coated with trichloro (1*H*,1*H*,2*H*,2*H*-perfluorooctyl silane) (Sigma) atop the soft silicone mold, and delivering PA solution with a syringe controlled the shape and thickness of the PA films (Fig. S18, ESI†). A flat PA film sealed to a 3D-square PA capping structure defined the encapsulation for the cathode. Punching holes (World Precision Instruments) into the PA cap formed a gateway between the electrodes. Centering the cathode on the PA film, applying a liquid mixture of PA solution around the perimeter, placing the cap on top of the liquid solution and illuminating with UV light completed the encapsulation structure. Subsequent synthesis of a ChCl/urea-based ionic liquid following a previously reported protocol[59] required heating 1 : 2 moles of choline chloride (Sigma) and urea at 80 °C, followed by adding $ZnCl_2$ at a 0.3 M concentration, to yield a clear, viscous eutectic solvent as the ionic liquid. Injecting this material into the PA pouch through the holes prevented rapid leakage of iodine upon exposure to biofluids or ground water.

Electrochemical measurements

An electrochemical potentiostat (Palmsens4, Palmsens) equipped with PSTrace software served as the basis for all electrochemical measurements.

Materials characterization and dissolution measurements

Morphological and compositional analyses relied on scanning electron microscopy (SEM, Hitachi SU 8030). Dissolution experiments involved immersion in PBS at 37 °C, 85 °C or implantation in chicken breast tissue, also immersed in PBS at 37 °C. Changing the buffer daily simulated physiological conditions. Image capture used an iPhone 13 Pro.

UV-vis spectroscopy

Rhodamine B was used in the PA pouch with two holes to represent the iodine. The ionic liquid and PBS were filled into the pouches, respectively. The pouch was then soaked into a vial filled with PBS. At regular time intervals, ~3 mL of PBS was drawn from the vial for UV-vis spectroscopy, which was thereafter returned to the vial after each measurement. The concentration of Rhodamine B was determined by measuring the absorption peak at 554 nm in the UV-vis spectrophotometer (HP8452, Agilent Technologies).

Simulations

The software Ansys Maxwell enable modeling of the distributions of current density. Use of an adaptive mesh (tetrahedron elements) ensured computational accuracy. The relative permittivity (ε_r) and bulk conductivity (σ) were 80 and 1.4 S m^{-1} for PBS, 10 and 0.0036 S m^{-1} for ionic liquid, and 1 and 3.3 S m^{-1} for the cathode composite. The electromagnetic parameters of other materials relied on the material library in the Ansys Maxwell software package.

Animals

All procedures adhered to the ethical standards and protocols of Northwestern University and conformed to the Guide for the Care and Use of Laboratory Animals.

In vivo electrochemical measurements

Stainless steel liquid flux (Worthington Inc.) exposed the insulated tips of a 2-channel electrode (invivo1). Silver epoxy joined the cells to insulated wires (5 cm in length) sealed in silicone tubing. A layer of PA coated the connection between the 2-channel electrode and cell as electrical insulation.

All procedures began with the provision of general anesthesia through isoflurane vapor (~2.5%), followed by pre-operative analgesia (SQ: ~1 mg kg^{-1} Meloxicam, line block of 0.25% Bupivacaine). Under sterile conditions, incisions were made on the skull and the lower intrascapular region. A subcutaneous tunnel connected the incisions to inset the sterilized device beneath. The skull was cleaned, the headpiece (2 channel electrode; invivo1) was fixed using LockTite glue and dental cement, and incisions were closed with a suture. Rats received post-op analgesia (~0.024 mg kg^{-1} Buprenorphine) immediately afterward and were provisioned additional doses of meloxicam 24 h post-surgery. Adult male Sprague-Dawley rats were used. Rats were individually housed at ~25 °C on a typical 12 h light 12 h dark cycle and monitored 24 h for the first day, then 2–3 times weekly to ensure wellbeing. Electrochemical measurements were captured using a Palmsens4 while the animal was awake and freely moving by connecting a commutator (invivo1) to the 2-channel electrode.

Biocompatibility studies

All procedures began with the provision of general anesthesia through isoflurane vapor (~2.5%), followed by pre-operative analgesia (SQ: ~1.2 mg kg^{-1} Meloxicam). A 1 cm transverse

incision was made on the flank at the peak of the bend of the spine. Sterilized samples of the eco/bioresorbable cell (anode, cathode, IL), cathode only, and PA control were placed subcutaneously in the interscapular region of male CD-1 mice, at least 5 mm cranial to the incision. Mice received post-op analgesia ($\sim$0.75 mg kg^{-1} Buprenorphine SR) and were provisioned additional doses of meloxicam 24 h post-surgery.

Daily checks and regular weighing certified safe conditions in male CD-1 mice. Blood was collected at 1 and 4 week endpoints to evaluate blood chemistry. The Veterinary Diagnostic Lab at the University of Illinois conducted the assays.

A necropsy examination was performed at 1 and 4 week timepoints on male CD-1 mice and included evaluation of external surfaces and orifices, body condition, musculoskeletal system, and major body cavities with their associated organs and tissues. Body weights and select organ weights were recorded at necropsy. Representative samples of brain, heart, lung, liver, spleen, and kidney with the surrounding tissue were collected from all animals and preserved in 10% neutral-buffered formalin. The formalin-fixed tissues were processed routinely and prepared for microscopic examination by embedding in paraffin, sectioning, mounting on glass slides, and staining with hematoxylin and eosin (H&E). A 5-grade scoring system was used to record the histopathology severity and included scores of minimal, mild, moderate, marked, and severe for gradable findings.

Fabrication of the pacing module (microcontroller approach)

Commercial computer-aided design (CAD) software (AutoCAD, AUTODESK) generated the circuit design. A laminate composite film of copper/polyimide/copper (18 μm/75 μm/18 μm, Pyralux, DuPont Inc.) served as the substrate. An ultraviolet laser system (Protolaser U4, LPKF) patterned the copper to define the traces, bond pads, and unplanted vias. Washing in stainless steel liquid flux (Worthington Inc), deionized water, and isopropanol (Fisher Scientific) prepared the resulting flexible printed circuit board (fPCB) for placement of electrical components by removing surface oxides. A non-conductive epoxy (Loctite 3621, Henkel) mechanically bonded these components to the fPCB. Reflow soldering with low-temperature solder paste (4900P SAC305, MG Chemicals) established electrical contact between the components (microcontroller, capacitor, resistors, and LEDs) and the copper pads.

In vivo pacing

All procedures began with the provision of general anesthesia through isoflurane vapor ($\sim$2.5%). A ventilator (VentElite; Harvard Apparatus) supplied oxygen during surgery. A left thoracotomy exposed the heart, and monofilament polypropylene sutures (Ethicon, 8705H) attached molybdenum electrodes on the myocardial surface of the left ventricle. A Palmsens4 equipped with PSTrace software captured ECG signals using subdermal needle electrodes positioned in the Lead I placement (positive on the right forelimb, negative on the left forelimb, and ground on the bottom left hind leg). Setting the stimulation at a higher frequency than the intrinsic heart rhythm enabled cardiac pacing. C57BL/6 mice were used. The bioresorbable Mo pacing electrodes were fabricated following a previously reported protocol.[69]

Fabrication of resistive temperature sensors and heating elements

Fabrication of temperature sensors began with spin casting a thin layer ($\sim$250 nm) of poly(methyl)methacrylate onto a 500 μm thick, polished mechanical-grade Si wafer followed by curing at 180 °C for 3 minutes. Next, a precursor to polyimide, poly(amic)acid, spin cast onto the sample produced film of polyimide ($\sim$1.5 μm thick) after curing for 30 s at 90 °C, 5 min at 150 °C, and 1 h under vacuum at 250 °C. Electron-beam evaporation of 10 nm Cr/100 nm Au followed by photolithography and wet chemical etching formed patterns to define the sensors and heaters. An additional layer of polyimide cast on top and patterned using photolithography and oxygen plasma etching (200 W, 200 mTorr, 25 sccm) served as electrical insulation. Immersion in acetone released the structures from the wafer, to allow transfer onto a water-soluble poly(vinyl)alcohol (PVA) tape. Sputtering $\sim$75 nm of SiO_2 onto the backside of the structure and placing it in contact with a thin film of silicone elastomer (Ecoflex 00-30, Smooth-On, Inc.) after exposure to UV-induced ozone led to strong adhesion due to formation of interfacial chemical bonds. Dissolving the PVA tape in water completed the process.

Fabrication of the temperature sensing BLE module

Commercial electronic design automation (EDA) software (EAGLE ver. 9.6.1, AUTODESK) generated the circuit schematic and design for the outsourced fPCBs. Multiple washes in deionized water and isopropanol (Fisher Scientific) removed surface oxides to prepare the fPCB for assembly. A non-conductive epoxy (Loctite 3621, Henkel) mechanically bonded the surface mount components to the fPCB) and reflow soldering (Weller WTHA1N, Weller Tools) with low-temperature solder paste (4900P SAC305, MG Chemicals) established electrical contact between the BLE SoC (ISP 1807, Insight SiP), power management integrated circuit (NPM1100, Nordic Semiconductor), temperature sensing integrated circuits (TMP117, Texas Instruments), IMU (LSM6DSO, ST Microelectronics), other associated passive components, and the fPCB. An iPad (iPad Mini, Apple) collected streamed data from the BLE module.

Statistical analysis

Results correspond to mean $\pm$ SD, unless otherwise stated. Graphpad Prism 9 enabled statistical analyses. A Welch ANOVA statistical test compared organ weights between eco/bioresorbable cells, cathodes only, and control (PA) groups, where $P \leq 0.05$ was considered statistically significant.

Author contributions

Ivy Huang, Yamin Zhang: conceptualization, methodology, validation, formal analysis, investigation, data curation, writing – original draft, review and editing, visualization. Hany Arafa: resources. Shupeng Li: Software. Abraham Vazquez Guardado,

Wei Ouyang: resources. Fei Liu: investigation. Surabhi Madhvapathy, Joseph Woojin Song: resources. Andreas Tzavelis: formal analysis. Jacob Trueb: software. Yeonsik Choi: resources. Elizabeth Dempsey, Nayereh Ghoreishi-Haack, Iwona Stepien: investigation, data curation. Keith Bailey: formal analysis. Shuling Han, Zheng Jenny Zhang: investigation. Cameron Good: methodology. Yonggang Huang: supervision. Amay J. Bandodkar, John A. Rogers: conceptualization, writing – original draft, review and editing, supervision, project administration.

Conflicts of interest

There are no conflicts of interest to declare.

Acknowledgements

This work utilized the Nano Fabrication Facility (NUFAB) and EPIC facilities of Northwestern University's NUANCE Center, which receives support from the Soft and Hybrid Nanotechnology Experimental (SHyNE) resource (NSF ECCS-2025633), the International Institute for Nanotechnology (IIN), and Northwestern's MRSEC program (NSF DMR-1720139); the Keck Biophysics Facility, a shared resource of the Robert H. Lurie Comprehensive Cancer Center of Northwestern University supported in part by the NCI Cancer Center Support Grant #P30 CA060553.

References

1 Federal Consortium for Advanced Batteries, *Executive Summary: National Blueprint for Lithium Batteries 2021–2030*, 2021.
2 F. Arshad, L. Li, K. Amin, E. Fan, N. Manurkar, A. Ahmad, J. Yang, F. Wu and R. Chen, *ACS Sustainable Chem. Eng.*, 2020, **8**, 13527–13554.
3 G. Harper, R. Sommerville, E. Kendrick, L. Driscoll, P. Slater, R. Stolkin, A. Walton, P. Christensen, O. Heidrich, S. Lambert, A. Abbott, K. Ryder, L. Gaines and P. Anderson, *Nature*, 2019, **575**, 75–86.
4 D. H. P. Kang, M. Chen and O. A. Ogunseitan, *Environ. Sci. Technol.*, 2013, **47**, 5495–5503.
5 A. Nedjalkov, J. Meyer, M. Köhring, A. Doering, M. Angelmahr, S. Dahle, A. Sander, A. Fischer and W. Schade, *Batteries*, 2016, **2**, 5.
6 J. Hou, L. Lu, L. Wang, A. Ohma, D. Ren, X. Feng, Y. Li, Y. Li, I. Ootani, X. Han, W. Ren, X. He, Y. Nitta and M. Ouyang, *Nat. Commun.*, 2020, **11**, 5100.
7 D. Chao, W. Zhou, F. Xie, C. Ye, H. Li, M. Jaroniec and S.-Z. Qiao, *Sci. Adv.*, 2020, **6**, 1–19.
8 United States Department of Health and Human Services, Toxicological Profile for Manganese, 2012.
9 A. Amar, A. Kouki and H. Cao, *Sensors*, 2015, **15**, 28889–28914.
10 Y. Choi, J. Koo and J. A. Rogers, *MRS Bull.*, 2020, **45**, 103–112.
11 S.-K. Kang, R. K. J. Murphy, S.-W. Hwang, S. M. Lee, D. V. Harburg, N. A. Krueger, J. Shin, P. Gamble, H. Cheng, S. Yu, Z. Liu, J. G. McCall, M. Stephen, H. Ying, J. Kim, G. Park, R. C. Webb, C. H. Lee, S. Chung, D. S. Wie, A. D. Gujar, B. Vemulapalli, A. H. Kim, K.-M. Lee, J. Cheng, Y. Huang, S. H. Lee, P. V. Braun, W. Z. Ray and J. A. Rogers, *Nature*, 2016, **530**, 71–76.
12 D. Lu, S. Li, Q. Yang, H. M. Arafa, Y. Xu, Y. Yan, D. Ostojich, W. Bai, H. Guo, C. Wu, S. Li, L. Jacobson, A. M. Westman, M. R. MacEwan, Y. Huang, M. Pet and J. A. Rogers, *Biosens. Bioelectron.*, 2022, **206**, 114145.
13 S. Yang, V. Sencadas, S. S. You, N. Z. Jia, S. S. Srinivasan, H. Huang, A. E. Ahmed, J. Y. Liang and G. Traverso, *Adv. Funct. Mater.*, 2021, **31**, 2009289.
14 S. Stauss and I. Honma, *Bull. Chem. Soc. Jpn.*, 2018, **91**, 492–505.
15 K. K. Fu, Z. Wang, J. Dai, M. Carter and L. Hu, *Chem. Mater.*, 2016, **28**, 3527–3539.
16 L. Yin, H. Cheng, S. Mao, R. Haasch, Y. Liu, X. Xie, S. Hwang, H. Jain, S. Kang, Y. Su, R. Li, Y. Huang and J. A. Rogers, *Adv. Funct. Mater.*, 2014, **24**, 645–658.
17 S.-W. Hwang, H. Tao, D.-H. Kim, H. Cheng, J.-K. Song, E. Rill, M. A. Brenckle, B. Panilaitis, S. M. Won, Y.-S. Kim, Y. M. Song, K. J. Yu, A. Ameen, R. Li, Y. Su, M. Yang, D. L. Kaplan, M. R. Zakin, M. J. Slepian, Y. Huang, F. G. Omenetto and J. A. Rogers, *Science*, 2012, **337**, 1640–1644.
18 N. Mittal, A. Ojanguren, M. Niederberger and E. Lizundia, *Adv. Sci.*, 2021, **8**, 2004814.
19 Y. J. Kim, W. Wu, S.-E. Chun, J. F. Whitacre and C. J. Bettinger, *Proc. Natl. Acad. Sci. U. S. A.*, 2013, **110**, 20912–20917.
20 L. Yin, X. Huang, H. Xu, Y. Zhang, J. Lam, J. Cheng and J. A. Rogers, *Adv. Mater.*, 2014, **26**, 3879–3884.
21 X. Huang, D. Wang, Z. Yuan, W. Xie, Y. Wu, R. Li, Y. Zhao, D. Luo, L. Cen, B. Chen, H. Wu, H. Xu, X. Sheng, M. Zhang, L. Zhao and L. Yin, *Small*, 2018, **14**, 1800994.
22 M. Tsang, A. Armutlulu, A. W. Martinez, S. A. B. Allen and M. G. Allen, *Microsyst. Nanoeng.*, 2015, **1**, 15024.
23 P. Nadeau, D. El-Damak, D. Glettig, Y. L. Kong, S. Mo, C. Cleveland, L. Booth, N. Roxhed, R. Langer, A. P. Chandrakasan and G. Traverso, *Nat. Biomed. Eng.*, 2017, **1**, 0022.
24 Y. J. Kim, S.-E. Chun, J. Whitacre and C. J. Bettinger, *J. Mater. Chem. B*, 2013, **1**, 3781.
25 L. Wang, C. Lu, S. Yang, P. Sun, Y. Wang, Y. Guan, S. Liu, D. Cheng, H. Meng, Q. Wang, J. He, H. Hou, H. Li, W. Lu, Y. Zhao, J. Wang, Y. Zhu, Y. Li, D. Luo, T. Li, H. Chen, S. Wang, X. Sheng, W. Xiong, X. Wang, J. Peng and L. Yin, *Sci. Adv.*, 2020, **6**, 1–15.
26 X. Jia, C. Wang, V. Ranganathan, B. Napier, C. Yu, Y. Chao, M. Forsyth, F. G. Omenetto, D. R. MacFarlane and G. G. Wallace, *ACS Energy Lett.*, 2017, **2**, 831–836.
27 M. H. Lee, J. Lee, S. Jung, D. Kang, M. S. Park, G. D. Cha, K. W. Cho, J. Song, S. Moon, Y. S. Yun, S. J. Kim, Y. W. Lim, D. Kim and K. Kang, *Adv. Mater.*, 2021, **33**, 2004902.
28 H. Tian, T. Gao, X. Li, X. Wang, C. Luo, X. Fan, C. Yang, L. Suo, Z. Ma, W. Han and C. Wang, *Nat. Commun.*, 2017, **8**, 14083.

29 S. Yagi, T. Ichitsubo, Y. Shirai, S. Yanai, T. Doi, K. Murase and E. Matsubara, *J. Mater. Chem. A*, 2014, **2**, 1144–1149.
30 H. Li, T. Ichitsubo, S. Yagi and E. Matsubara, *J. Mater. Chem. A*, 2017, **5**, 3534–3540.
31 A. J. Bandodkar, S. P. Lee, I. Huang, W. Li, S. Wang, C.-J. Su, W. J. Jeang, T. Hang, S. Mehta, N. Nyberg, P. Gutruf, J. Choi, J. Koo, J. T. Reeder, R. Tseng, R. Ghaffari and J. A. Rogers, *Nat. Electron.*, 2020, **3**, 554–562.
32 H. Wang, L. Jiang, H. Wu, W. Zheng, D. Kan, R. Cheng, J. Yan, C. Yu and S.-K. Sun, *ACS Biomater. Sci. Eng.*, 2019, **5**, 3654–3662.
33 A. Ilin and A. Nersesyan, *Arch. Oncol.*, 2013, **21**, 65–71.
34 H. Tsuchiya, T. Shirai, H. Nishida, H. Murakami, T. Kabata, N. Yamamoto, K. Watanabe and J. Nakase, *J. Orthop. Sci.*, 2012, **17**, 595–604.
35 J. Vormann, *Mol. Aspects Med.*, 2003, **24**, 27–37.
36 R. J. Elin, *Am. J. Clin. Pathol.*, 1994, **102**, 616–622.
37 F. Witte, *Acta Biomater.*, 2010, **6**, 1680–1692.
38 M. P. Staiger, A. M. Pietak, J. Huadmai and G. Dias, *Biomaterials*, 2006, **27**, 1728–1734.
39 L. Mao, L. Shen, J. Chen, X. Zhang, M. Kwak, Y. Wu, R. Fan, L. Zhang, J. Pei, G. Yuan, C. Song, J. Ge and W. Ding, *Sci. Rep.*, 2017, **7**, 46343.
40 P. Chakraborty Banerjee, S. Al-Saadi, L. Choudhary, S. E. Harandi and R. Singh, *Materials*, 2019, **12**, 136.
41 Z. Wang, M. U. Hassan, F. Nadeem, L. Wu, F. Zhang and X. Li, *Front. Plant Sci.*, 2020, **10**, 1–10.
42 Q. Dou, Y. Wang, A. Wang, M. Ye, R. Hou, Y. Lu, L. Su, S. Shi, H. Zhang and X. Yan, *Sci. Bull.*, 2020, **65**, 1812–1822.
43 E. Sheha, F. Liu, T. Wang, M. Farrag, J. Liu, N. Yacout, M. A. Kebede, N. Sharma and L.-Z. Fan, *ACS Appl. Energy Mater.*, 2020, **3**, 5882–5892.
44 J. Medrano-Macías, P. Leija-Martínez, S. González-Morales, A. Juárez-Maldonado and A. Benavides-Mendoza, *Front. Plant Sci.*, 2016, **7**, 1–20.
45 Y. S. Choi, J. Koo, Y. J. Lee, G. Lee, R. Avila, H. Ying, J. Reeder, L. Hambitzer, K. Im, J. Kim, K. Lee, J. Cheng, Y. Huang, S. Kang and J. A. Rogers, *Adv. Funct. Mater.*, 2020, **30**, 2000941.
46 D. Katti, S. Lakshmi, R. Langer and C. Laurencin, *Adv. Drug Delivery Rev.*, 2002, **54**, 933–961.
47 Q. Wen, J.-X. Chen, Y.-L. Tang, J. Wang and Z. Yang, *Chemosphere*, 2015, **132**, 63–69.
48 D. Jung, J. B. Jung, S. Kang, K. Li, I. Hwang, J. H. Jeong, H. S. Kim and J. Lee, *Green Chem.*, 2021, **23**, 1300–1311.
49 D. of H. and H. S. Food and Drug Administration, Fed. Regist., 2016, 81, 33741–33999.
50 National Institutes of Health, Iodine: Fact Sheet for Consumers, **https://ods.od.nih.gov/factsheets/Iodine-Consumer/**.
51 J. Cheng, B. Liu, Y. H. Wu and Y. F. Zheng, *J. Mater. Sci. Technol.*, 2013, **29**, 619–627.
52 MilliporeSigma, Safety data sheet: Tetraethylene glycol dimethyl ether, **https://www.emdmillipore.com/US/en/product/Tetraethylene-glycol-dimethyl-ether,MDA_CHEM-820959**.
53 MilliporeSigma, Safety data sheet: Magnesium bis(hexamethyldisilazide), **https://www.sigmaaldrich.com/US/en/sds/aldrich/692352**.
54 B. R. Puri and R. C. Bansal, *Carbon*, 1965, **3**, 227–230.
55 S. Moulay, *J. Polym. Eng.*, 2013, **33**, 389–443.
56 L. Bargnesi, F. Gigli, N. Albanelli, C. Toigo and C. Arbizzani, *Nanomaterials*, 2022, **12**, 254.
57 Y. Chen, N. Liu, H. Shao, W. Wang, M. Gao, C. Li, H. Zhang, A. Wang and Y. Huang, *J. Mater. Chem. A*, 2015, **3**, 15235–15240.
58 Q. Li, E. T. Dunn, E. W. Grandmaison and M. F. A. Goosen, *J. Bioact. Compat. Polym.*, 1992, **7**, 370–397.
59 W. Kao-ian, R. Pornprasertsuk, P. Thamyongkit, T. Maiyalagan and S. Kheawhom, *J. Electrochem. Soc.*, 2019, **166**, A1063–A1069.
60 S.-K. Kang, S.-W. Hwang, S. Yu, J.-H. Seo, E. A. Corbin, J. Shin, D. S. Wie, R. Bashir, Z. Ma and J. A. Rogers, *Adv. Funct. Mater.*, 2015, **25**, 1789–1797.
61 L. Yin, J. Scharf, J. Ma, J.-M. Doux, C. Redquest, V. L. Le, Y. Yin, J. Ortega, X. Wei, J. Wang and Y. S. Meng, *Joule*, 2021, **5**, 228–248.
62 G. Lee, Y. S. Choi, H.-J. Yoon and J. A. Rogers, *Matter*, 2020, **3**, 1031–1052.
63 C. W. Park, S.-K. Kang, H. L. Hernandez, J. A. Kaitz, D. S. Wie, J. Shin, O. P. Lee, N. R. Sottos, J. S. Moore, J. A. Rogers and S. R. White, *Adv. Mater.*, 2015, **27**, 3783–3788.
64 H. L. Hernandez, S.-K. Kang, O. P. Lee, S.-W. Hwang, J. A. Kaitz, B. Inci, C. W. Park, S. Chung, N. R. Sottos, J. S. Moore, J. A. Rogers and S. R. White, *Adv. Mater.*, 2014, **26**, 7637–7642.
65 M. Xing, Z. Z. Zhao, Y. J. Zhang, J. W. Zhao, G. L. Cui and J. H. Dai, *Mater. Today Energy*, 2020, **18**, 100534.
66 M. Razavi, M. Fathi, O. Savabi, L. Tayebi and D. Vashaee, *Materials*, 2020, **13**, 1315.
67 J. Kuhlmann, I. Bartsch, E. Willbold, S. Schuchardt, O. Holz, N. Hort, D. Höche, W. R. Heineman and F. Witte, *Acta Biomater.*, 2013, **9**, 8714–8721.
68 J. Koo, S. B. Kim, Y. S. Choi, Z. Xie, A. J. Bandodkar, J. Khalifeh, Y. Yan, H. Kim, M. K. Pezhouh, K. Doty, G. Lee, Y.-Y. Chen, S. M. Lee, D. D'Andrea, K. Jung, K. Lee, K. Li, S. Jo, H. Wang, J.-H. Kim, J. Kim, S.-G. Choi, W. J. Jang, Y. S. Oh, I. Park, S. S. Kwak, J.-H. Park, D. Hong, X. Feng, C.-H. Lee, A. Banks, C. Leal, H. M. Lee, Y. Huang, C. K. Franz, W. Z. Ray, M. MacEwan, S.-K. Kang and J. A. Rogers, *Sci. Adv.*, 2022, **6**, eabb1093.
69 Y. S. Choi, R. T. Yin, A. Pfenniger, J. Koo, R. Avila, K. Benjamin Lee, S. W. Chen, G. Lee, G. Li, Y. Qiao, A. Murillo-Berlioz, A. Kiss, S. Han, S. M. Lee, C. Li, Z. Xie, Y.-Y. Chen, A. Burrell, B. Geist, H. Jeong, J. Kim, H.-J. Yoon, A. Banks, S.-K. Kang, Z. J. Zhang, C. R. Haney, A. V. Sahakian, D. Johnson, T. Efimova, Y. Huang, G. D. Trachiotis, B. P. Knight, R. K. Arora, I. R. Efimov and J. A. Rogers, *Nat. Biotechnol.*, 2021, **39**, 1228–1238.
70 P. Gutruf, R. T. Yin, K. B. Lee, J. Ausra, J. A. Brennan, Y. Qiao, Z. Xie, R. Peralta, O. Talarico, A. Murillo, S. W. Chen, J. P. Leshock, C. R. Haney, E. A. Waters, C. Zhang, H. Luan, Y. Huang, G. Trachiotis, I. R. Efimov and J. A. Rogers, *Nat. Commun.*, 2019, **10**, 5742.
71 S. K. Mulpuru, M. Madhavan, C. J. McLeod, Y.-M. Cha and P. A. Friedman, *J. Am. Coll. Cardiol.*, 2017, **69**, 189–210.

72 C. Dagdeviren, B. D. Yang, Y. Su, P. L. Tran, P. Joe, E. Anderson, J. Xia, V. Doraiswamy, B. Dehdashti, X. Feng, B. Lu, R. Poston, Z. Khalpey, R. Ghaffari, Y. Huang, M. J. Slepian and J. A. Rogers, *Proc. Natl. Acad. Sci. U. S. A.*, 2014, **111**, 1927–1932.

73 H. P. Kok, E. N. K. Cressman, W. Ceelen, C. L. Brace, R. Ivkov, H. Grüll, G. ter Haar, P. Wust and J. Crezee, *Int. J. Hyperth.*, 2020, **37**, 711–741.

74 M. W. Dewhirst, Z. Vujaskovic, E. Jones and D. Thrall, *Int. J. Hyperth.*, 2005, **21**, 779–790.

75 S. R. Madhvapathy, Y. Ma, M. Patel, S. Krishnan, C. Wei, Y. Li, S. Xu, X. Feng, Y. Huang and J. A. Rogers, *Adv. Funct. Mater.*, 2018, **28**, 1802083.

76 S. R. Madhvapathy, H. Wang, J. Kong, M. Zhang, J. Y. Lee, J. Bin Park, H. Jang, Z. Xie, J. Cao, R. Avila, C. Wei, V. D'Angelo, J. Zhu, H. U. Chung, S. Coughlin, M. Patel, J. Winograd, J. Lim, A. Banks, S. Xu, Y. Huang and J. A. Rogers, *Sci. Adv.*, 2020, **6**, 1–12.

77 S. R. Krishnan, H. M. Arafa, K. Kwon, Y. Deng, C.-J. Su, J. T. Reeder, J. Freudman, I. Stankiewicz, H.-M. Chen, R. Loza, M. Mims, M. Mims, K. Lee, Z. Abecassis, A. Banks, D. Ostojich, M. Patel, H. Wang, K. Börekçi, J. Rosenow, M. Tate, Y. Huang, T. Alden, M. B. Potts, A. B. Ayer and J. A. Rogers, *npj Digit. Med.*, 2020, **3**, 29.

78 R. C. Webb, A. P. Bonifas, A. Behnaz, Y. Zhang, K. J. Yu, H. Cheng, M. Shi, Z. Bian, Z. Liu, Y.-S. Kim, W.-H. Yeo, J. S. Park, J. Song, Y. Li, Y. Huang, A. M. Gorbach and J. A. Rogers, *Nat. Mater.*, 2013, **12**, 938–944.

79 R. C. Webb, Y. Ma, S. Krishnan, Y. Li, S. Yoon, X. Guo, X. Feng, Y. Shi, M. Seidel, N. H. Cho, J. Kurniawan, J. Ahad, N. Sheth, J. Kim, J. G. Taylor VI, T. Darlington, K. Chang, W. Huang, J. Ayers, A. Gruebele, R. M. Pielak, M. J. Slepian, Y. Huang, A. M. Gorbach and J. A. Rogers, *Sci. Adv.*, 2015, **1**, 1–13.

80 H. Arkin, L. X. Xu and K. R. Holmes, *IEEE Trans. Biomed. Eng.*, 1994, **41**, 97–107.

81 J. W. Valvano, J. R. Cochran and K. R. Diller, *Int. J. Thermophys.*, 1985, **6**, 301–311.

82 M. Elwenspoek, in *CAS '99 Proceedings. 1999 International Semiconductor Conference (Cat. No. 99TH8389)*, IEEE, 1999, vol. 2, pp. 423–435.

